International Journal of Solids and Structures 129 (2017) 103–118

Contents lists available at ScienceDirect

International Journal of Solids and Structures

journal homepage: www.elsevier.com/locate/ijsolstr

Elastic-plastic modeling of metallic strands and wire ropes under axial tension and torsion loads

L. Xiang [a,b], H.Y. Wang [a,b], Y. Chen [a,b], Y.J. Guan [c], L.H. Dai [a,b,*]

[a] State Key Laboratory of Nonlinear Mechanics, Institute of Mechanics, Chinese Academy of Sciences, Beijing 100190, China
[b] School of Engineering Science, University of Chinese Academy of Sciences, Beijing 101408, China
[c] Materials Genome Center, Beijing Institute of Aeronautical Materials, Beijing, 100095, China

ARTICLE INFO

Article history:
Received 16 March 2017
Revised 22 June 2017
Available online 8 September 2017

Keywords:
Elastic-plastic behavior
Straight strand
Multi-strand rope
Yielding and failure
Wire contact
Local strain measurement

ABSTRACT

Elastic-plastic response is greatly involved in the failure of wire ropes. Based on the derivation of the local deformation parameters of individual wire, an analytical model characterizing the elastic-plastic behavior for both wire strands and multi-strand ropes is developed in this paper. Also, the contact status within a multilayered strand is carefully studied to achieve a full understanding of wire stresses. Details of the surface strain fields of ropes are captured by 3D digital image correlation (3D-DIC) technique and the results agree well with the prediction of the present model. Varying loading conditions are considered to analyze the yielding and failure behavior of wire strands. It is found that the rotation of ropes (no matter its positive or negative) will increase the overall stress level over the wire cross section, however, restraining the rope ends leads to higher contact stress. Increasing the helix angle moderately may be an effective method to reduce the contact pressure of strand wires. Our model provides straightforward prediction of the elastic-plastic response of wire ropes and proves an effective tool for rope design due to a great reduction of time consuming in numerical simulations.

1. Introduction

Steel wire ropes, which are constructed from either a single straight strand or from several strands that are wound around a core, have been widely used as structural elements due to their high axial strength and bending flexibility. For instance, wire ropes are widely used in cranes, elevator lifting, suspension bridges, and aerial rope ways. The security service of wire ropes is one of the most concerns to engineering. In the past century, a great effort has been devoted to develop analytical models and experimental works for the mechanical response of the wire ropes. Reviews were given by Cardou and Jolicoeur (1997), Feyrer (2007) and lately by Spak et al. (2013).

The early models assume a fibrous response of each wire and ignore its bending and torsion rigidity, which were introduced by Hruska (1952a,b) and Lanteigne (1985). Based on the nonlinear equations of equilibrium of curved rods (Love, 1944), Costello and Phillips (1976) presented a thin rod model considering the bending and torsion stiffness of the wires. Utting and Jones (1987a,b) have extended the Costello's analysis to include wire flattening (contact deformation) and friction effects and the model presents a good prediction of cable stiffness with their experimental results. Velinsky et al. (1984) extended the thin rod model to complex multi-strand rope configuration by treating a wound strand as being a wire. Elata et al. (2004) fully considered the double-helix configuration in multi-strand ropes and fiber assumption was taken to simplify the analysis procedure. Ghoreishi et al. (2007) carried out a comparative study between diverse analytical models by a full 3D finite element model of a 7-wire strand. They found that there is a negligible difference between analytical models for straight strands whose lay angles are above 70°. Stanova et al., (2011a,b) introduced a mathematical model for both the single-helix and the double-helix configurations in the form of parametric equations. Their method presents high efficiency in building the finite element model of wire ropes. Usabiaga and Pagalday (2008) and Xiang et al. (2015) developed two other models for multi-strand cables, on the basis of the general thin rod theory (Love, 1944). They take infinite friction and frictionless assumption hypothesis respectively and the local deformation along wires of the two kinematics shows great difference. Recently, Foti and Martinelli (2016c) presented a model for metallic strands subjected to tension, torsion and bending loads, which fully considered the hysteretic bending behavior and the residual contact forces due to the stranding process.

* Corresponding author at: State Key Laboratory of Nonlinear Mechanics, Institute of Mechanics, Chinese Academy of Sciences, Beijing 100190, China
E-mail address: lhdai@lnm.imech.ac.cn (L.H. Dai).

http://dx.doi.org/10.1016/j.ijsolstr.2017.09.008
0020-7683/

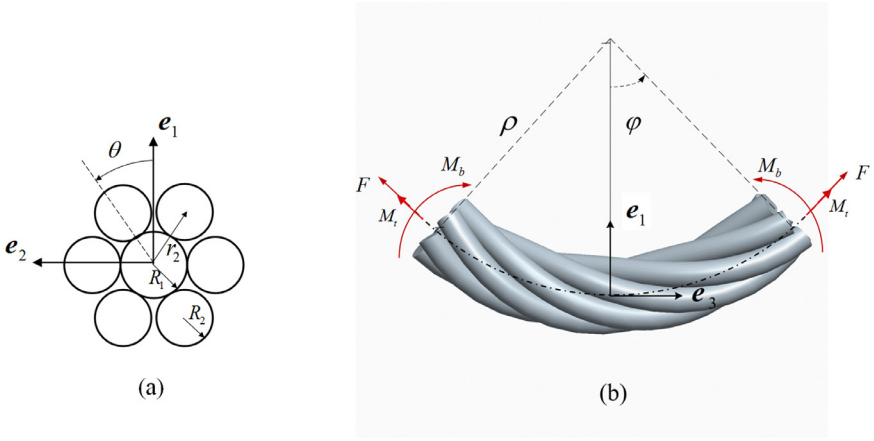

Fig. 1. Tension, torsion and bending of a 1×7 simple strand.

In addition, the contact status of straight strands has been studied by some researchers. Based on the Hertz elastic contact theory, Kumar et al. (1997) and Kumar and Botsis (2001) calculated the contact stresses of a simple strand with a fibrous core and multilayered strands subjected to axial tension and torsion respectively. Gnanavel et al. (2010) and Gnanavel and Parthasarathy (2011, 2012) studied the coupled contact performance (an outer wire generates full contact with the center wire and the adjacent outer wires) of a straight strand and the influence of friction was taken into consideration. Argatov (2011) developed a mathematical model for a wire strand that detailedly considered the transverse contraction through Poisson's ratio and also through local contact deformations (wire flattening). It is shown that the effect of elastic local deformations in the frictionless interwire contact interactions is relatively small for large lay angles (more than 75°), while for small lay angles (less than 65°), the wire flattening effect dominates the Poisson's ratio effect. Analogously, Meng et al. (2016) studied the effect of core-wire contact on mechanical performance of wire strands based on a semi-analytical method and their results agree well with the Hertz contact theory.

The above models mainly lead to an elastic deformation analysis. However, the elastic-plastic responses of the wires are important to predict the rope yielding and failure behavior. Frigerio et al. (2016) found that internal stresses lead to local plastification even for a nominal stress level far below the yield strength of the material, because of residual stresses from the manufacturing process. In order to establish the damage evolution, such as the wear of the wires, the elastic-plastic contact status of rope wires also need to be carefully clarified. Nevertheless, the current elastic-plastic models of wire ropes are usually based on the finite element analysis. Not much analytical work has been done for characterizing the elastic-plastic behavior of wire ropes.

In the paper of Erdonmez and Imrak (2011), a finite element modeling procedure is introduced to get the elastic-plastic response of a typical 7×7 wire rope. Judge et al. (2012) also developed a 3D elastic-plastic finite element to illustrate the behavior of spiral strands, especially localized yielding and plastic hardening in wires and mechanisms of final cable failure. Fontanari et al. (2015) studied the elastic-plastic behavior of a Warrington-Seale rope and the load distribution among the wires is given by their simulation. In order to save the computation time, Jiang et al. (1999) took advantage of the helical symmetry features and created a concise finite element model for wire strands, and later they used the model to analyze statically indeterminate contacts of strand wires in axially loaded situation (Jiang et al., 2008). Páczelt and Beleznai (2011) developed the p-version finite element software to improve the calculation efficiency of contacts in a simple straight two-layered strand.

In general, finite element models have high computation cost so numerical models always simulate only one-sixth or shorter pitch length of the rope (especially for multi-strand cables), which is far away from the situation that they were used in realistic structures. This may lead to insufficient contact between wires, and incorrect stresses across the rope cross section, which are influenced by the boundary condition at the rope end. Also contact between wires is prevalent in ropes and accurate analysis of contact stresses needs a rather high density of elements. For saving the computation time, usually the authors take two contact wires out of the rope structure to study the wire contact and wear problem directly. Lévesque et al. (2011) and Wang et al. (2013) adopted the sub-modeling approach in ABAQUS software to get accurate elastic-plastic contact stresses between two wires in strands, whose principle is to use the solution of a global model in order to establish the boundary conditions of a sub-model in which the area of interest is contained and further mesh refinement can be implemented. Meanwhile, Cruzado et al. (2013, 2014) directly refined the mesh of contact area to explore the wear damage evolution in the wire surface. However, one should use the actual contact parameters (for instance, contact force and the radius of curvature of the contact surface) derived from the stressed wire ropes to get a real response of the wires, which requires a combination of the theoretical contact analysis and the numerical simulation to deal with the nonlinear elastic-plastic contact problem within a rope.

The few analytical results for the elastic-plastic response of metallic strands are obtained by Foti and de Luca di Roseto (2016a) recently. Based on the theoretical description of Foti and Martinelli (2016c), a simple 1×6 strand under axial-torsional loads was taken into consideration and a 3D finite element model was also proposed. The results of the proposed analytical formulation agree well with experimental and theoretical results from the literature (Utting and Jones, 1987b; Costello, 1990) and their numerical simulation. The contact results are not directly given by the authors and the elastic-plastic behavior of multi-strand wire ropes needs to be further studied as well, since most wire ropes in practical use have a complex multi-strand cross-section (Argatov, 2011) and the geometrical and mechanical property of the double-helix wires in multi-strand ropes differs much from the single-helix wires in straight strands (Lee, 1991).

In this paper, an analytical method is proposed to obtain the elastic-plastic deformation of both simple strands and multi-strand ropes. The present model is based on the thin rod theory of Love (1944) and the frictionless assumption. In order to get the elastic–plastic stress, the strain through the wire cross is calculated

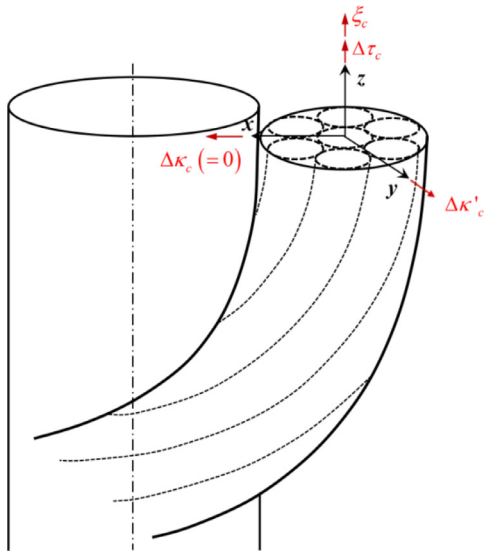

Fig. 2. Take an outer strand as an outer wire (the strand is subjected to tension, torsion and bending simultaneously).

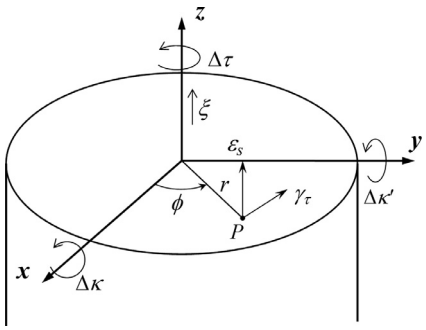

Fig. 3. Deformation through a wire cross section.

first via the derivation of the local tension, bending and torsion deformation parameters of wires. Then the elastic–plastic model for straight strands is built by a typical numerical approach to plasticity and the response of multi-strand ropes is obtained by treating an outer strand as a single-helix outer wire.

The paper is organized as follows. Section 2 gives the basic geometrical description of a strand subjected to tension, torsion and bending simultaneously and how to deal with a multi-strand wire rope. Section 3 describes the analytical model to determine elastic–plastic response of strands and ropes, including the overall strain and stress prediction and the local contact analysis. Experimental tests on individual wires and surface strain measurement of ropes through 3D-DIC are presented in Section 4. Results from our elastic–plastic model, comparisons with experimental data and analyses of stresses under different conditions are reported in Section 5. And finally Section 6 summarizes the whole paper and gives the main conclusions.

2. Geometrical description of strands and ropes

2.1. Tension, torsion and bending of a simple strand

For a straight strand (Fig. 1), the initial centerline of a wound wire is given by the following parametric equations:

$$x_1 = r_2 \cos(\theta + \theta_0) \tag{1a}$$

$$x_2 = r_2 \sin(\theta + \theta_0) \tag{1b}$$

$$x_3 = r_2 \tan\alpha_2 \theta \tag{1c}$$

where r_2 is the laying radius of the outer wire, α_2 is the laying angle, θ is a free parameter representing the angle of the centerline spiral around the axis of the rope and θ_0 is the wire phase angle indicating the wire position relative to $\boldsymbol{e}_1$ when $x_3 = 0$.

Consider now the strand with length h subjected to an axial elongation Δu and a rotation angle $\Delta\phi$, the tensile strain ε_t and the angle of twist per unit length τ_t are respectively defined as

$$\varepsilon_t = \frac{\Delta u}{h} \tag{2a}$$

$$\tau_t = \frac{\Delta\phi}{h} \tag{2b}$$

The location along the stressed centerline of a strand wire can be expressed by equations (Usabiaga and Pagalday, 2008):

$$x_1' = r_2 \cos(\theta + \theta_0 + \tau_t x_3) \tag{3a}$$

$$x_2' = r_2 \sin(\theta + \theta_0 + \tau_t x_3) \tag{3b}$$

$$x_3' = x_3 + \varepsilon_t x_3 \tag{3c}$$

Next, when the same prestresssed strand is subjected to bending with a radius of curvature ρ, As illustrated in Fig. 1, the centerline of the strand axis is given by the following equations:

$$x_{1,c} = \rho \cdot (1 - \cos\varphi) \tag{4a}$$

$$x_{2,c} = 0 \tag{4b}$$

$$x_{3,c} = \rho \sin\varphi \tag{4c}$$

where $\varphi = \frac{x_3'}{\rho}$ and the subscript 'c' represents the center wire.

The well-known Frenet–Serret local frame $\{\boldsymbol{n}, \boldsymbol{b}, \boldsymbol{t}\}$ is used to describe the deformed configuration. Here $\boldsymbol{t}$ is the tangent unit vector along the tangential direction of the centerline, $\boldsymbol{n}$ is the principal normal and $\boldsymbol{b}$ is the binormal vector. For the central wire of the bending strand

$$\boldsymbol{n}_c = (\cos\varphi,\ 0,\ -\sin\varphi)^T \tag{5a}$$

$$\boldsymbol{b}_c = (0,\ 1,\ 0)^T \tag{5b}$$

$$\boldsymbol{t}_c = (\sin\varphi,\ 0,\ cos\varphi)^T \tag{5c}$$

Then projecting the wire point to the local frame $\{\boldsymbol{n}_c, \boldsymbol{b}_c, \boldsymbol{t}_c\}$, we can get the centerline of the strand outer wire now:

$$x_{1,b} = \rho(1 - \cos\varphi) + r_2 \cos\overline{\theta}\cos\varphi \tag{6a}$$

$$x_{2,b} = r_2 \sin\overline{\theta} \tag{6b}$$

$$x_{3,b} = \rho\sin\varphi - r_2 \cos\overline{\theta}\sin\varphi \tag{6c}$$

where $\overline{\theta} = \theta + \theta_0 + \tau_t x_3$ representing the angle of an outer wire spiral around the axis of the strand after torsion, since τ_t is the angle of twist in strand per unit length and x_3 is the coordinate along the lengthwise direction.

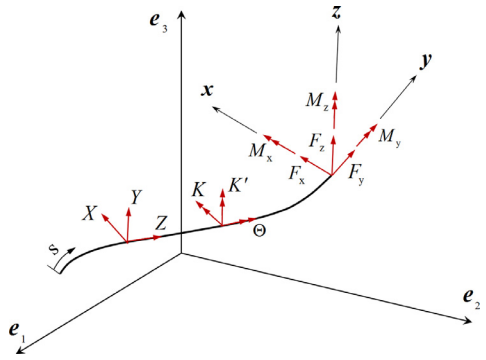

Fig. 4. Forces and moments acting on a wire (after Costello, 1990).

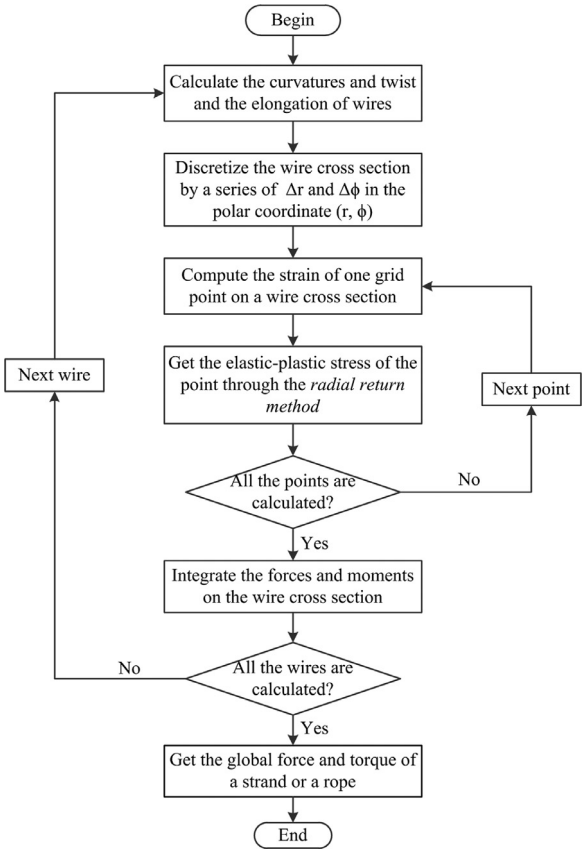

Fig. 5. The flowchart of the elastic–plastic solution process.

2.2. Multi-strand ropes subjected to axial tension and torsion

Consider a multi-strand wire rope, consisting of several strands that are wound around a core, and in turn each strand has a helical structure consisting of several wires. By treating each strand as a helix wire, the rope's mechanical behavior is just like a straight strand. The similar homogenization procedure was also adopted by (Costello, 1990) to get the mechanical characteristics of multi-strand wire ropes.

When a multi-strand rope is subjected to axial tension and torsion, each spiral strand undergoes not only tension and torsion along its centerline but also bending against the rope core. As the wires in the strand have been treated as a whole, the external deformation of the strand can be described by the kinematics parameters of its central wire (Fig. 2). The central wire of an outer strand is a single-helix wire and the variations of curvatures and twist of the wire can be derived as:

$$\Delta\kappa_c = 0 \tag{7a}$$

$$\Delta\kappa_c' = \frac{\cos^2\alpha_c'}{r_c'} - \frac{\cos^2\alpha_c}{r_c} \tag{7b}$$

$$\Delta\tau_c = \frac{\sin\alpha_c' \cos\alpha_c'}{r_c'} - \frac{\sin\alpha_c \cos\alpha_c}{r_c} \tag{7c}$$

where the superscript ' ' ' represents the deformed state. The helix angle α_c' and radius r_c' after deformation has been derived by Costello (1990), and so does the tensile strain ξ_c. Then the tensile strain ξ_{strand}, the twist τ_{strand} and the bending radius ρ_{strand} of the strand are: $\xi_{strand} = \xi_c$, $\tau_{strand} = \Delta\tau_c$ and $\rho_{strand} = 1/|\Delta\kappa'_c|$.

Then, the interpretation of an outer strand in a multi-strand rope is analogous the description of a strand subjected to tension, torsion and bending simultaneously in Section 2.1.

3. The elastic–plastic mechanical model

3.1. The elastic-plastic analysis of ropes

The wire deformation can be expressed with four parameters: elongation (ξ), twist (τ) and bending curvatures (κ and κ'). Love (1944) introduced the *principal torsion-flexure axes* {***x***, ***y***, ***z***} to compute curvatures κ and κ' and the twist τ, which is an orthonormal local frame that always stick to the wire cross section and varies along with the deformation of the wire. It indicates a one-to-one corresponding relationship between the material points in the undeformed and deformed state. When the axes are fully determined, the deformation parameters can be calculated by

$$\kappa = l_3\frac{dl_2}{ds} + m_3\frac{dm_2}{ds} + n_3\frac{dn_2}{ds} \tag{8a}$$

$$\kappa' = l_1\frac{dl_3}{ds} + m_1\frac{dm_3}{ds} + n_1\frac{dn_3}{ds} \tag{8b}$$

$$\tau = l_2\frac{dl_1}{ds} + m_2\frac{dm_1}{ds} + n_2\frac{dn_1}{ds} \tag{8c}$$

where, for example, l_1, m_1, n_1 are the direction cosines of the axis ***x***.

In the initial configuration, the selection of the *principal torsion-flexure axes* has some arbitrariness. Usually we make the axes equivalent to the Frenet-Serret axes to simplify the computation. That is

$$\{\boldsymbol{x}_0, \boldsymbol{y}_0, \boldsymbol{z}_0\} = \{\boldsymbol{n}_0, \boldsymbol{b}_0, \boldsymbol{t}_0\} \tag{9}$$

where the subscript '0' represents the undeformed state.

When the strand is subjected to external load, we suppose that the wire cross section rotates rigidly with the cross section of the strand, which is also a basic assumption taken by Usabiaga and Pagalday (2008) and Foti and Martinelli (2016c). As clarified by Xiang et al. (2015), $\boldsymbol{n}_0$ (i.e. $\boldsymbol{x}_0$) always points to the center of the initial strand. So after deformation the unit vector ***x*** is still along the line from the wire centroid to the strand center in a cable cross section. Therefore,

$$\boldsymbol{x} = \{\boldsymbol{n}_c, \boldsymbol{b}_c, \boldsymbol{t}_c\}^T \begin{Bmatrix} -\cos\bar{\theta} \\ -\sin\bar{\theta} \\ 0 \end{Bmatrix} \tag{10}$$

As ***z*** is always collinear to the tangent vector of the centreline of the wire, so

$$\boldsymbol{z} = \boldsymbol{t} \tag{11}$$

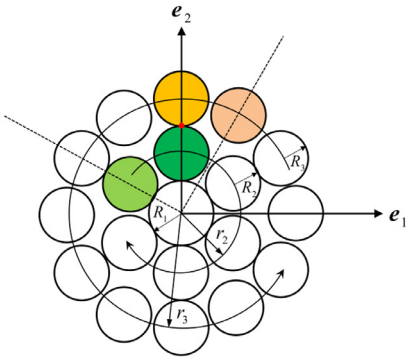

(a) Initial point contact of an outer and an inner wire

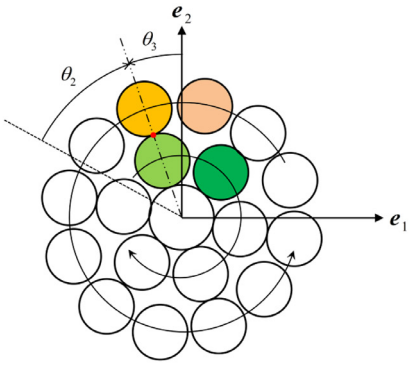

(b) Next point contact location of an outer wire

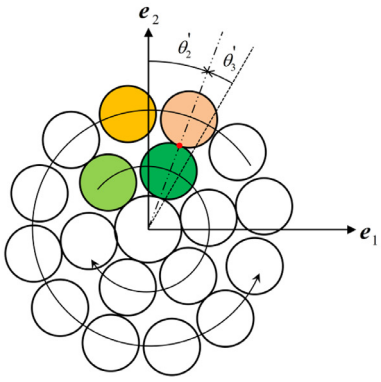

(c) Next point contact location of an inner wire

Fig. 6. Point contact description within wires of the 1×19 strand.

and finally

$$\boldsymbol{y} = \boldsymbol{z} \times \boldsymbol{x} \tag{12}$$

Then the *principal torsion-flexure axes* after deformation is determined by Eqs. (10) to (12) and the variation of the curvatures $\Delta\kappa$ and $\Delta\kappa'$ and the twist $\Delta\tau$ can be obtained by comparing the values before and after deformation via Eq. (7).

The elongation ξ is derived from the length change of the wire. Usually the wire length varies with the tension, torsion and bending of the strand. However, due to the frictionless hypothesis we considered in this paper, the bending contribution to the axial strain of the wires is equal to zero as the wire can slide freely to keep its length unchanged (Foti and Martinelli, 2016b). So ξ results from total tension ε_t and total torsion τ_t of the strand. That

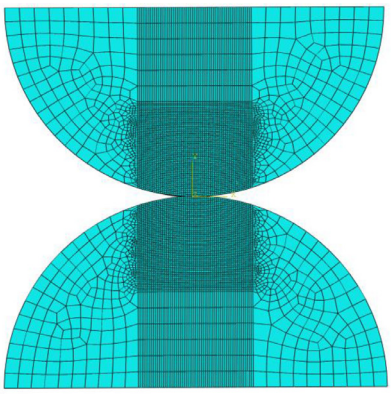

(a) Mesh of the contact model

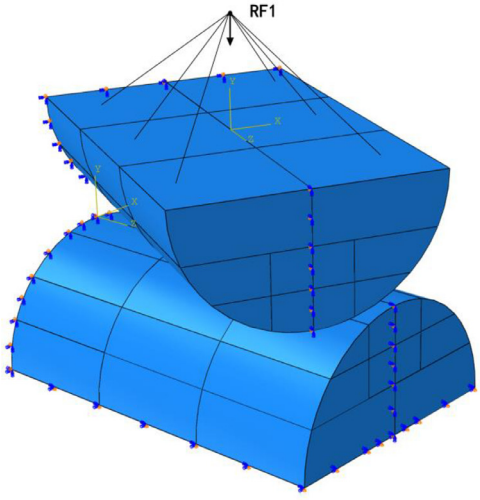

(b) Load and boundary conditions

Fig. 7. Contact model of the FEM simulation.

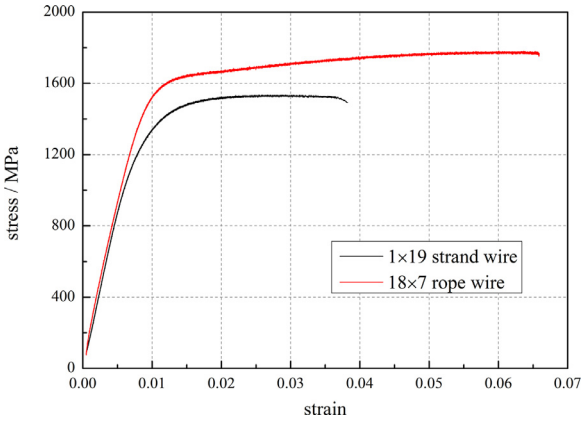

Fig. 8. Stress strain σ - ε curves of the different wires.

is (Xiang et al., 2015)

$$\xi = \frac{\sqrt{(1+\tau_t r_2 \tan\alpha_2)^2 + (\tan\alpha_2)^2(1+\varepsilon_t)^2}}{\sqrt{1+(\tan\alpha_2)^2}} - 1 \tag{13}$$

Consider a point $P(r, \phi)$ in the wire cross-section shown in Fig. 3, the strain-tensor matrix in the frame $\{\boldsymbol{x}, \boldsymbol{y}, \boldsymbol{z}\}$ can be written as

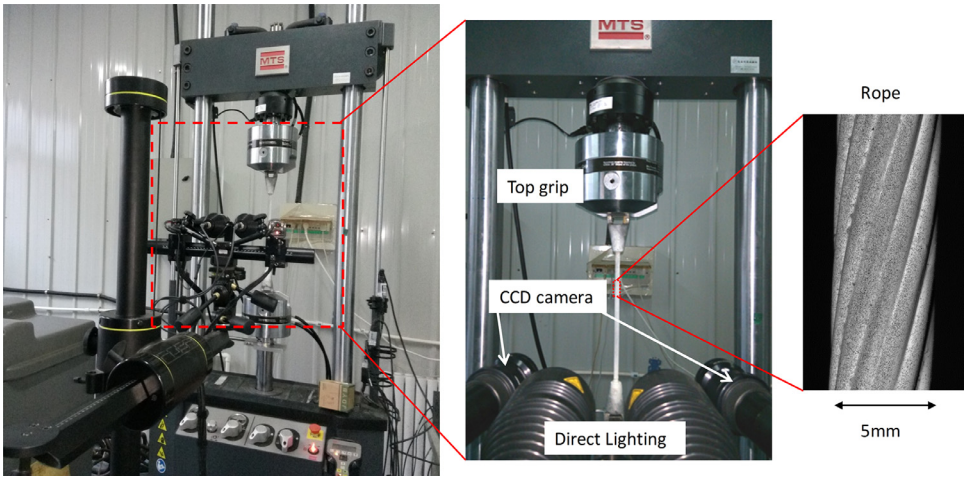

Fig. 9. Experimental setup of the 3D-DIC strain measurement of a rope surface.

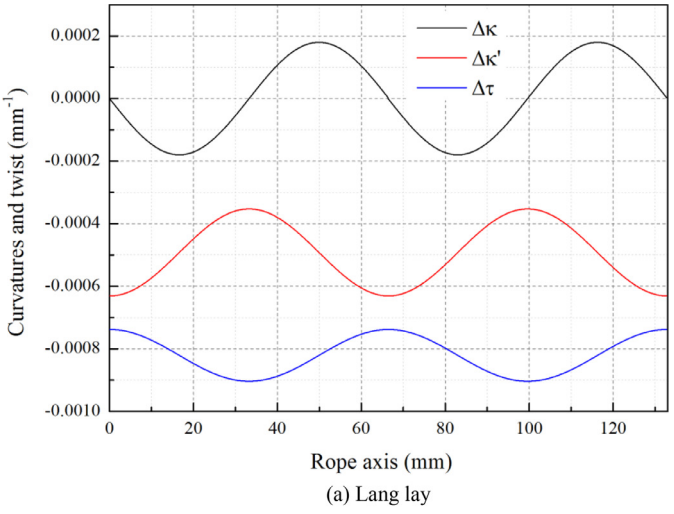

(a) Lang lay

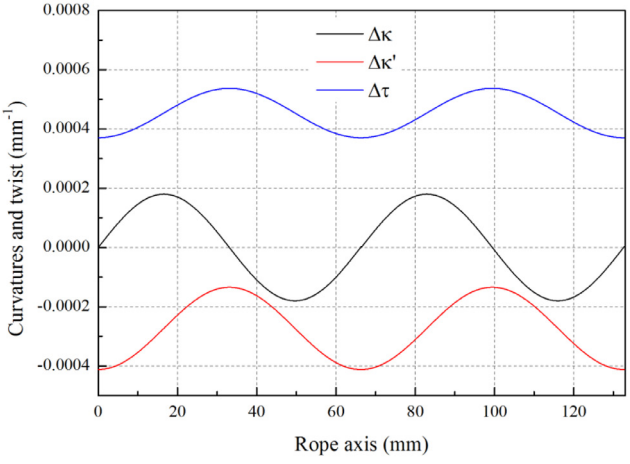

(b) Regular lay

Fig. 10. Local deformation parameters of outer wires in the outer strands of 7×7 ropes under $\varepsilon_t = 0.01$ and $\tau_t = 0$.

$$\boldsymbol{\varepsilon} = \begin{bmatrix} \varepsilon_{xx} & 0 & \varepsilon_{xz} \\ 0 & \varepsilon_{yy} & \varepsilon_{yz} \\ \varepsilon_{zx} & \varepsilon_{zy} & \varepsilon_{zz} \end{bmatrix} \tag{14}$$

and $\varepsilon_{xx} = \varepsilon_{yy} = -\nu\varepsilon_{zz}$.

Based on the hypothesis that a section initially normal to the wire centerline remains plane after deformation, the axial normal strain ε_s and the circumferential shear strain γ_τ can be driven from the variation values of four aforementioned deformation parameters: ξ, $\Delta\tau$, $\Delta\kappa$ and $\Delta\kappa'$. That is

$$\varepsilon_s = \Delta\kappa \cdot r\sin\phi - \Delta\kappa' \cdot rcos\phi + \xi \tag{15}$$

$$\gamma_\tau = r\Delta\tau \tag{16}$$

Then the component of strain-tensor $\boldsymbol{\varepsilon}$ is

$$\varepsilon_{zz} = \varepsilon_s \tag{17a}$$

$$\varepsilon_{xz} = -\frac{1}{2}\gamma_\tau \sin\phi \tag{17b}$$

$$\varepsilon_{yz} = \frac{1}{2}\gamma_\tau \cos\phi \tag{17c}$$

As for elastic-plastic behavior of the wire material, strains are assumed to be sufficiently small for the cross sections to remain plane, so that the strain-tensor is still presented as Eqs. (14) to (17) when yielding has happened on the wires. Usually the strain tensor $\boldsymbol{\varepsilon}$ can be decomposed into two parts, that is $\boldsymbol{\varepsilon} = \boldsymbol{\varepsilon}_e + \boldsymbol{\varepsilon}_p$, and the stress tensor $\boldsymbol{\sigma} = \mathbf{C}$: $(\boldsymbol{\varepsilon} - \boldsymbol{\varepsilon}_p)$. The Von Mises yield criterion is:

$$f(\boldsymbol{\sigma}) = \sqrt{3J_2(\boldsymbol{\sigma})} - \sigma_Y(\bar{\varepsilon}_p) \quad \leq \quad 0 \tag{18}$$

where $\bar{\varepsilon}_p$ represents the equivalent plastic strain and $\sigma_Y(\bar{\varepsilon}_p)$ is determined from a real elastic–plastic constitutive law. If the yield criterion is not satisfied, the increment of the plastic strain is

$$\Delta\boldsymbol{\varepsilon}_p = \delta\lambda\sqrt{\frac{3}{2}}\hat{\boldsymbol{n}} \tag{19}$$

where $\hat{\boldsymbol{n}} = \frac{dev(\boldsymbol{\sigma})}{\|dev(\boldsymbol{\sigma})\|}$. And λ is an internal variable which satisfies

$$\dot{\lambda} \geq 0, \quad \dot{\lambda} f = 0 \tag{20}$$

We use the well-known *radial return method* for von Mises plasticity (the reader is referred to Belytschko et al. (2000) for a detailed presentation) and the Newton-Raphson algorithm to solve the elastic-plastic increment steps. In order to ensure the computational accuracy, adequate density of points is considered along wire cross sections. The grid points are controlled by specifying the radial and angular discretization intervals Δr and $\Delta\phi$ in the polar coordinates of the wire cross section $(r,\ \phi)$. The exhibition of the final results is helped by the visualization procedure of ABAQUS

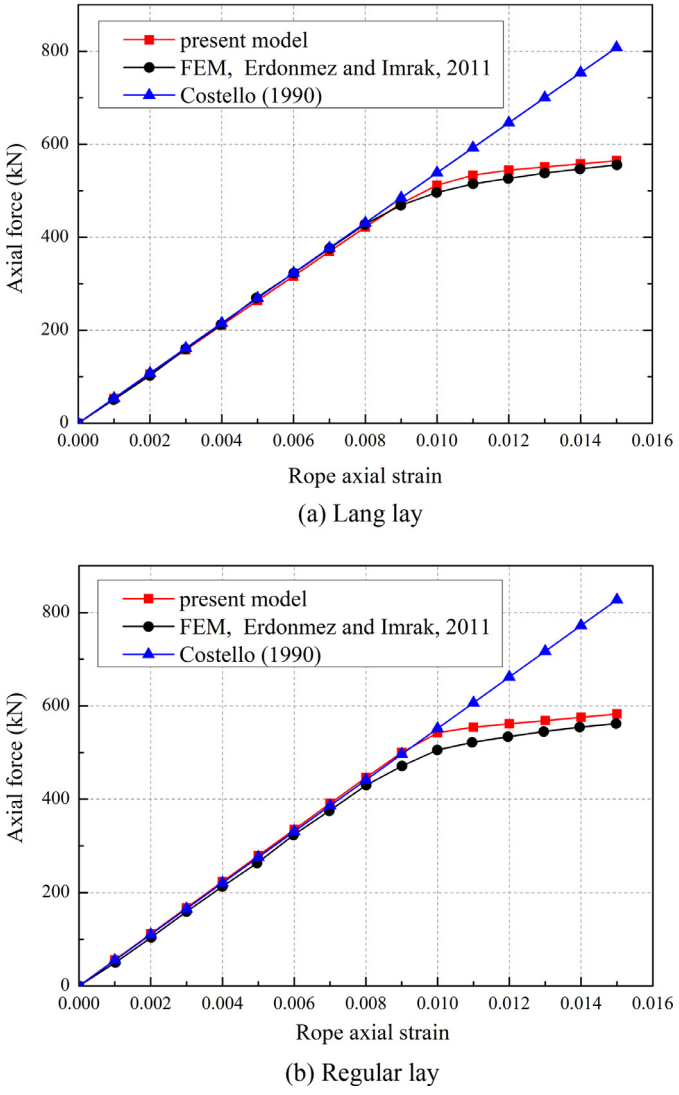

Fig. 11. Global tension of 7×7 ropes with different geometric structure.

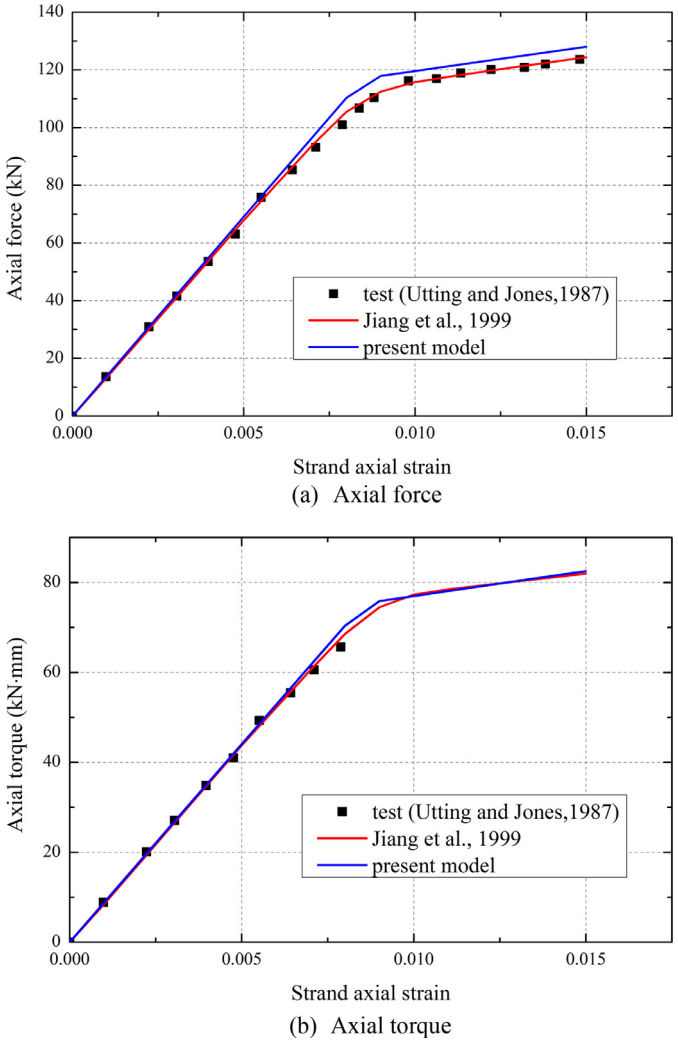

Fig. 12. Global tension of the 1×7 strand (fixed-end case).

software, i.e. strain and stress data of every point is converted to the form of the '.odb' file via the Python programming language.

After the elastic-plastic stress analysis, the local force F_z through the cross sectional area A is:

$$F_z = \int_A \sigma_{zz} dA \tag{21}$$

and the local moments are computed by virtue of

$$M_x = \int_A \sigma_{zz} r \sin\phi dA \tag{22a}$$

$$M_y = \int_A \sigma_{zz} r \cos\phi dA \tag{22b}$$

$$M_z = \int_A \sigma_{zy} r \cos\phi dA - \int_A \sigma_{zx} r \sin\phi dA \tag{22c}$$

The general case of loading on a wire is shown in Fig. 4. F_x, F_y and F_z are the forces along ***x, y*** and ***z*** directions respectively on a given cross section and M_x, M_y and M_z are the moments in ***x, y*** and ***z*** directions respectively. Considering the wire contact, there are forces, such as contact forces and moments that act on the outer surface of the wire. These distributed forces and moments are denoted by X, Y and Z and K, K' and Θ in ***x, y*** and ***z*** directions, respectively. Then we can get the following equilibrium equations:

$$\frac{dF_x}{ds} - F_y\tau + F_z\kappa' + X = 0 \tag{23a}$$

$$\frac{dF_y}{ds} - F_z\kappa + F_x\tau + Y = 0 \tag{23b}$$

$$\frac{dF_z}{ds} - F_x\kappa' + F_y\kappa + Z = 0 \tag{23c}$$

$$\frac{dM_x}{ds} - M_y\tau + M_z\kappa' - F_y + K = 0 \tag{23d}$$

$$\frac{dM_y}{ds} - M_z\kappa + M_x\tau + F_x + K' = 0 \tag{23e}$$

$$\frac{dM_z}{ds} - M_x\kappa' + M_y\kappa - \Theta = 0 \tag{23f}$$

So the force and moments in Eqs. (21) and (22) are computed from stresses at the grid points of every cross section by means of a standard numerical integration technique. And the forces F_x and F_y are directly calculated from Eqs. (23d) and (23e) as the contact moments K and K' can be neglected under the frictionless condition.

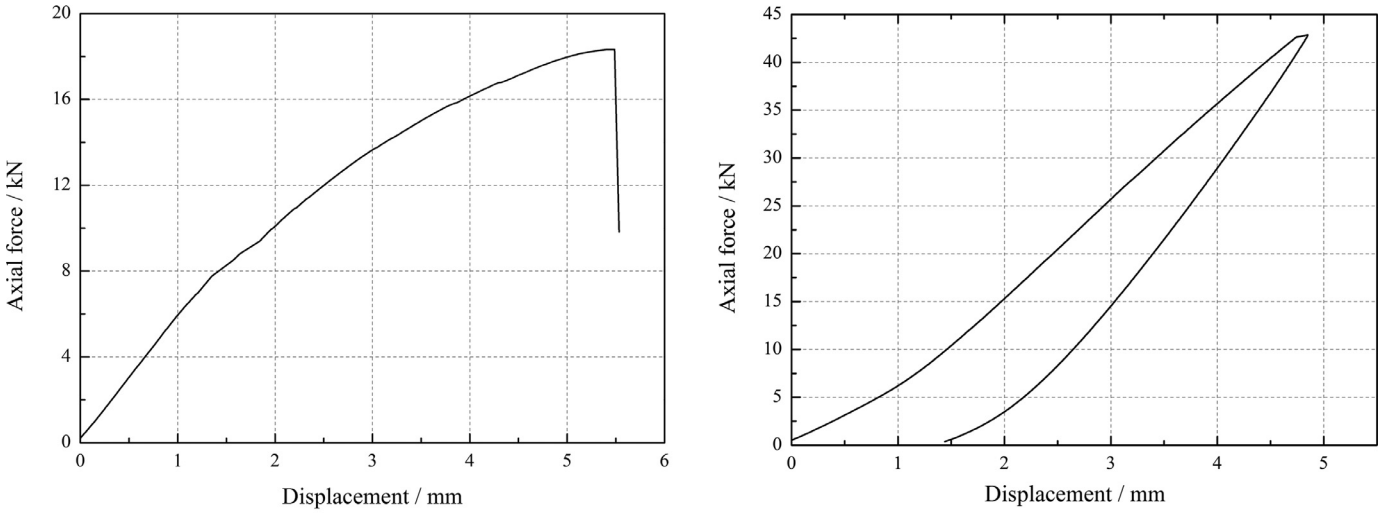

Fig. 13. Force-displacement curves of two different ropes.

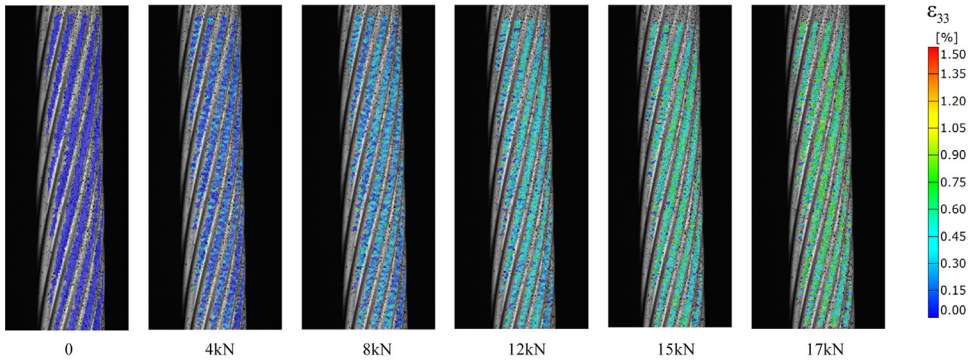

(a) Axial tension strain under different loading forces

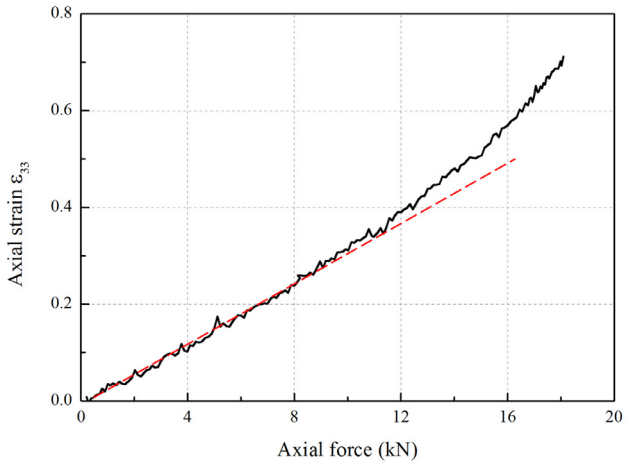

(b) Average axial strain vs. axial force

Fig. 14. Surface strain measurement of the 1 × 19 strand through 3D-DIC.

The contribution of a particular wire 'i' to the global response of the rope is made by projecting the local forces and moments of a wire cross section to the global coordinate system. That is

$$F_i = (F_x \cdot \boldsymbol{x} + F_y \cdot \boldsymbol{y} + F_z \cdot \boldsymbol{z}) \cdot \boldsymbol{e}_3 \tag{24a}$$

$$M_i = (\boldsymbol{\eta} \times F_x \cdot \boldsymbol{x} + \boldsymbol{\eta} \times F_y \cdot \boldsymbol{y} + \boldsymbol{\eta} \times F_z \cdot \boldsymbol{z} + M_x \cdot \boldsymbol{x} + M_y \cdot \boldsymbol{y} + M_z \cdot \boldsymbol{z}) \cdot \boldsymbol{e}_3 \tag{24b}$$

where $\boldsymbol{\eta}$ is the vector from the considered wire centroid to its nearest point on the rope central axis.

Then the total response of the rope can be computed by

$$F_t = F_c + \sum_1^n F_i \tag{25a}$$

$$M_t = M_{t,\,c} + \sum_1^n M_i \tag{25b}$$

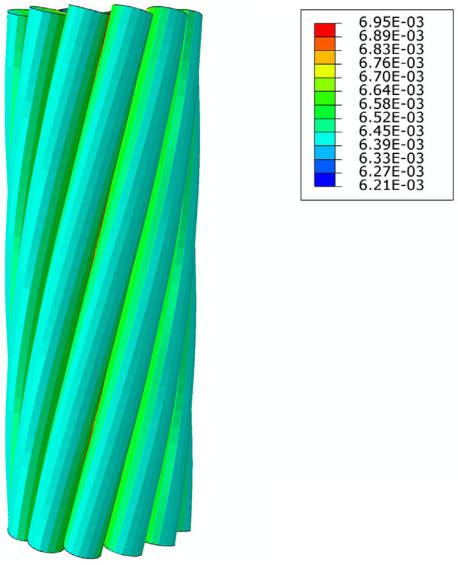

(a) The lateral view

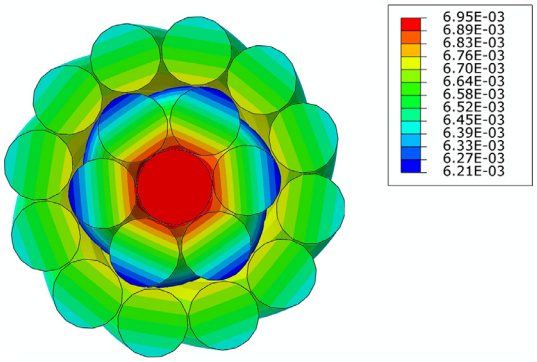

(b) The cross-section view

Fig. 15. Axial strain ε_{33} of the 1×19 strand under 17 kN predicted by the present model.

where the subscript 'c' represents the core wire, n is total number of other wires and F_t and M_t are the total tensile force and torque of the rope respectively.

3.2. The solution process of the elastic–plastic model

The flowchart of our elastic–plastic solution process is shown in Fig. 5, and the detailed numerical procedure is as follows:

Step 1. Calculate the curvatures and twist, and the elongation of wires. For a straight strand, the wires (except the core wire) are configured as single-helix and the local deformation parameters can be obtained directly. As for a multi-strand rope, the local curvatures and twist of the outer wires in its outer strands (double-helix wires) should be derived by treating an outer strand as a single-helix wire.

Step 2. Put adequate calculating points on wire cross sections by specifying the radial and angular discretization intervals Δr and $\Delta\phi$ in the polar coordinates of the wire cross section (r, ϕ).

Step 3. Compute the strain of one grid point on a wire cross section via Eqs. (14) to (17).

Step 4. Get the elastic-plastic stress of the point through the numerical algorithm for the incremental plasticity based on the *radial return method*.

Step 5. Judge whether the whole points on a wire cross section are calculated. If the above condition is satisfied, go to Step 6. Otherwise, prepare to deal with the next controlling point and go to Step 3.

Step 6. Get the forces and moments on wire cross sections through Eqs. (21) and (22) by means of a standard numerical integration technique.

Step 7. Judge whether all the wires are dealt with. If the above condition is satisfied, go to Step 8. Otherwise, prepare to compute the next wire and go to Step 1.

Step 8. Get the global force and torque of a strand or a rope by projecting the local forces and moments of every wire to the global coordinate system.

A particular example of a multi-strand wire rope under axial loads will be given later in Section 5.1 to help readers understand the computation process of the developed elastic-plastic model.

3.3. Contact analysis of metallic strands

Besides the overall stress prediction introduced above, the localized stress due to the contact interaction of the wires is critical to be considered since it may cause an eventual damage in the form of local yielding or wear, which is closely related to the fatigue and failure behavior of the wire rope. Usually two types of contact between the wires in two adjoining layers occurs: line contact and point contact (trellis contact), depending on the nature of their helix pattern in the same or opposite direction respectively. The lateral (or circumferential) contact between wires in the same layer is always ignored because of interlayer clearances (Feyrer, 2007) or manufacturing imperfections and strand ageing (Cardou and Jolicoeur, 1997), which has been elaborated in detail by Foti and Martinelli (2016c).

Consider a 1×6 simple strand that has been analyzed by many other researchers. As the circumferential contact has been neglected, the only contact mode is the line contact between the central and outside wires. Costello (1990) gives the contact force X_{c1} by apportion the distributed resultant force X_2 of an outer wire centerline to the contact helix line. That is

$$X_{c1} = -\frac{l_2}{l_{c1}} X_2 \tag{26}$$

where l_2 ($=2\pi r_2/\cos\alpha_2$) and l_{c1} ($=2\pi R_1/\cos\alpha_2$) are the length of the outer wire centerline and the contact line over one pitch respectively. And X_2 can be calculated from Eq. (23a) after the foregoing elastic-plastic analysis.

However, the contact status in multilayered strands is much more complex. We take a typical 1×19 wire strand including two layers with opposite helical direction into consideration. The cross section of the 1×19 strand with one center wire, m_2 inner layer wire ($m_2 = 6$) and m_3 outer layer wire ($m_3 = 12$) is shown in Fig. 6a. The core wire and the inner wire generate line contact while the outer wire and the inner wire generate point contact. Point contact does not appear everywhere so we need to know the number of contact points within every pitch of one specific wire. We focus our attention on the outer layer wire. In Fig. 6(a), a point contact just generates where the wires of every layer are located along the same radial direction. As wires rotating, the outer layer wire contacts with another inner layer wire (Fig. 6b) and they sweep the same length along the rope axis. We can obtain

$$\frac{\pi}{3} = \theta_2 + \theta_3 = \frac{2\pi}{m_2} \tag{27}$$

$$r_2 \tan\alpha_2 \theta_2 = r_3 \tan\alpha_3 \theta_3 \tag{28}$$

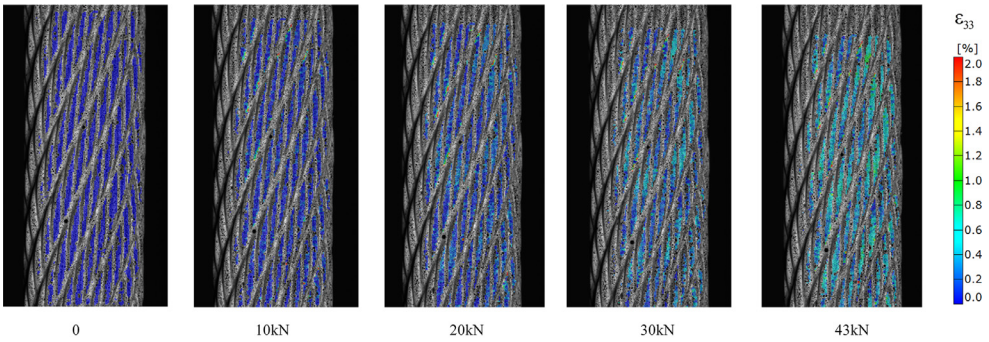

(a) Axial tension strain under different loading forces

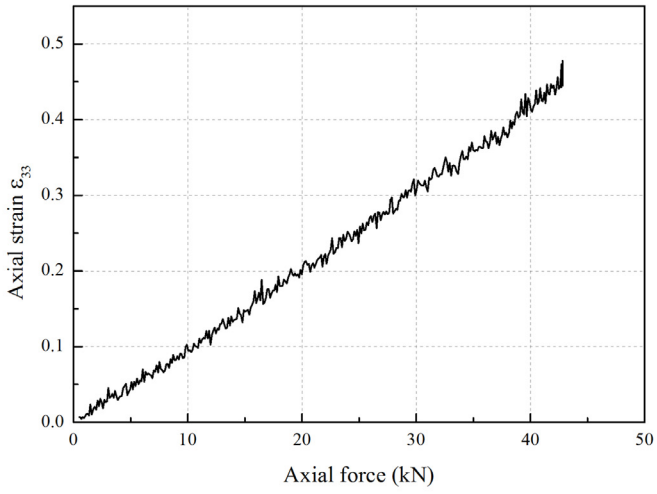

(b) Average axial strain vs. axial force

Fig. 16. Surface strain measurement of the 18 × 7 rope through 3D-DIC.

Table 1
Mechanical properties of the tested wire materials.

	1 × 19 strand wire	18 × 7 rope wire
Young's modulus (MPa)	178,310	171,179
Yield stress (MPa)	1305.4	1558.0
Limit stress (MPa)	1531.6	1781.1

Table 2
Main geometric parameters of the 1 × 7 simple strand and the 7 × 7 multi-strand rope.

Simple strand	
Center wire radius, R_1	1.97mm
Helix wire radius, R_2	1.865mm
Helix angle, $\boldsymbol{\alpha}_2$	78.2°
IWRC	
Core strand center wire radius, R_1	1.97mm
Core strand outer wire radius, R_2	1.865mm
Outer strand center wire radius, R_3	1.6mm
Outer strand outer wire radius, R_4	1.5mm
Core strand outer wire helix angle, $\boldsymbol{\alpha}_2$	71.01°
Outer strand center wire helix angle, $\boldsymbol{\alpha}_3$	71.46°
Outer strand outer wire helix angle, $\boldsymbol{\alpha}_4$	74.45°

So within one pitch, $2\pi/\theta_3$ contact points form along an outer layer wire.

The line load X_3 acting on the outer layer wire centerline results from the point contact forces between the inner and outer layer wires. We assume that the resultant line load X_3 distributes equally on the contact points (LeClair, 1991; Kumar and Botsis, 2001), so the point contact force $F_{c,point}$ is

$$F_{c,point} = \frac{X_3 l_3}{2\pi/\theta_3} \tag{29}$$

where l_3 ($=2\pi r_3/\cos\alpha_3$) is the length of the outer layer centerline over one pitch and X_3 can be computed from Eq. (23a).

Similarly, the number of contact points along an inner layer wire is $2\pi/\theta_2'$ (Fig. 6c) and θ_2' is determined by the following two formulae:

$$\frac{\pi}{6} = \theta_2' + \theta_3' = \frac{2\pi}{m_3} \tag{32}$$

$$r_2 \tan\alpha_2 \theta_2' = r_3 \tan\alpha_3 \theta_3' \tag{33}$$

Consider the force equilibrium on the centerline of an inner layer wire. Both the line contact force $f_{c,line}$ from the center wire and the point contact force $F_{c,point}$ from the outer layer wire act on the inner layer wire. So the force balance equation over one pitch is

$$f_{c,line} l_{c1} = X_2 l_2 + F_{c,point}\left(2\pi/\theta_2'\right) \tag{34}$$

Then the line contact force $f_{c,line}$ of the 1 × 19 strand can be obtained from Eq. (34).

Within the elastic region, the contact stress can be derived via the Hertz contact theory. However, when considering the elastic-plastic behavior of the wire material, an analytical solution is difficult to achieve due to its high nonlinearity. We will use the finite element method to get elastic-plastic contact stresses, which

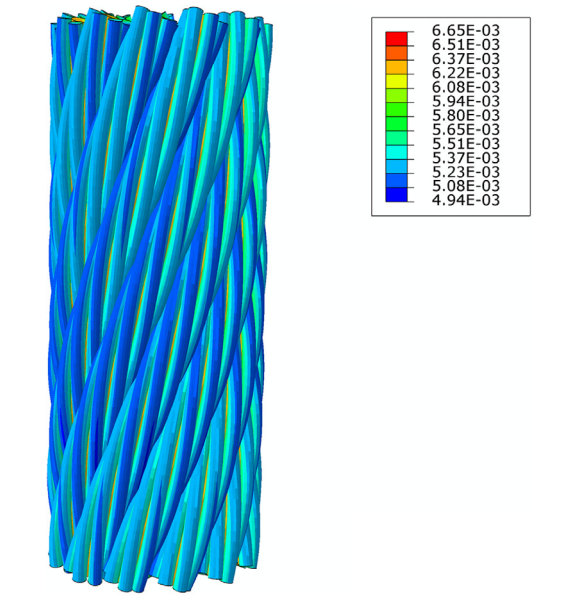

(a) The lateral view

(b) The cross-section view

Fig. 17. Axial strain ε_{33} of the 18×7 rope under 43 kN predicted by the present model.

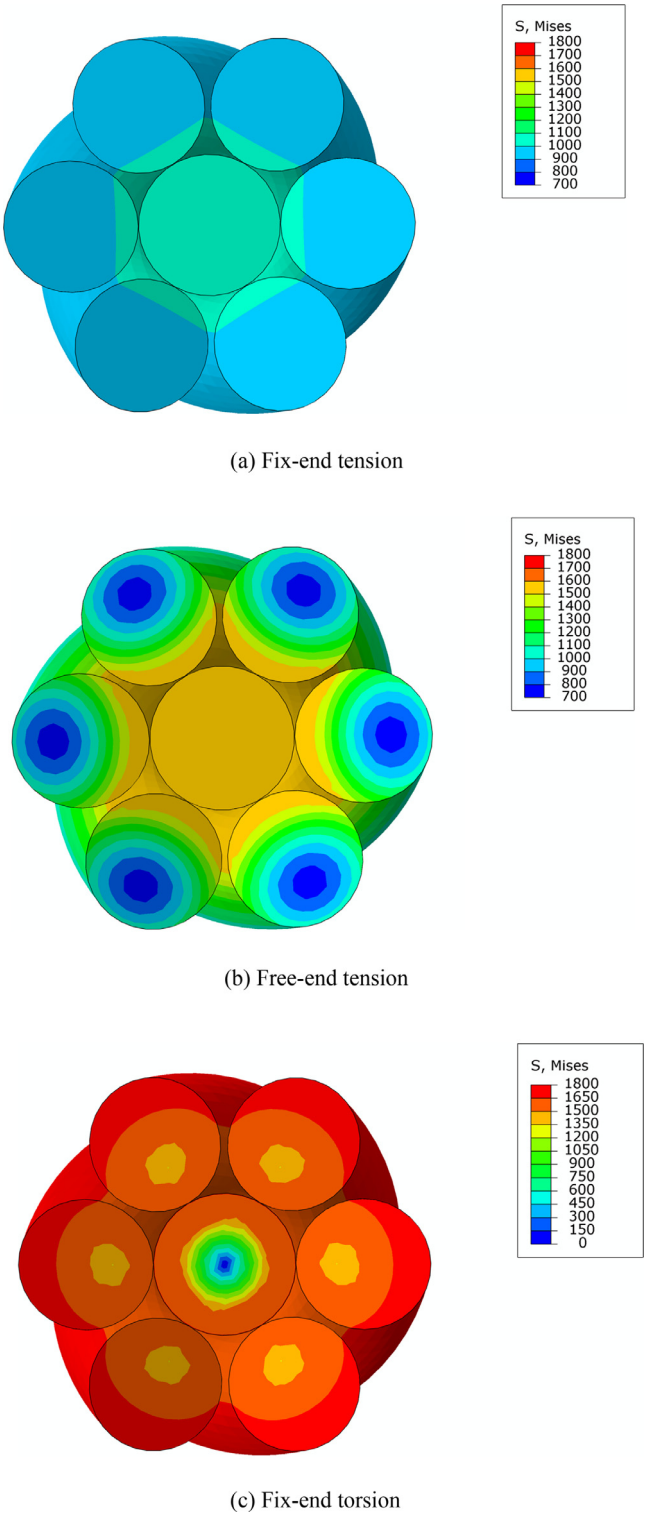

(a) Fix-end tension

(b) Free-end tension

(c) Fix-end torsion

Fig. 18. The Von Mises stress distribution of the 1×7 strand under 75 kN.

has been adopted by Lévesque et al. (2011), Wang et al. (2013) and Cruzado et al. (2013, 2014).

In this paper, ABAQUS software 6.10 is adopted to model the contact between two wires in a strand (Fig. 7). All the models are meshed with eight-node linear brick elements with reduced integration (C3D8R). Much more refined meshes are used in the contact zone to capture accurate values of contact pressures and stresses (Fig. 7a). The contact surface interaction between both cylinders is defined via the finite sliding contact pair algorithm, which uses the master-slave algorithm to enforce the contact constraints. The contact load is applied in the upper surface of the upper wire through the distributing coupling constraint, which concentrates the forces of nodes on the free surface to a reference node (Fig. 7b). One end of the two wires is fixed along the axial direction while the other is free. At the same time, a symmetrical boundary condition is applied on symmetry lines of every wire ends to prevent the wire rotation for ensuring the convergence of solving process.

4. Experimental tests

To verify our mode's validity, a 1×19 wire strand of 5 mm diameter and an 18×7 non-rotating rope of 10 mm diameter are tested. The elastic-plastic constitutive laws of the wires are identified by experiments and then used as input data for the proposed model. Then the results of our computation are compared to the surface strains of the ropes measured through 3D-DIC method.

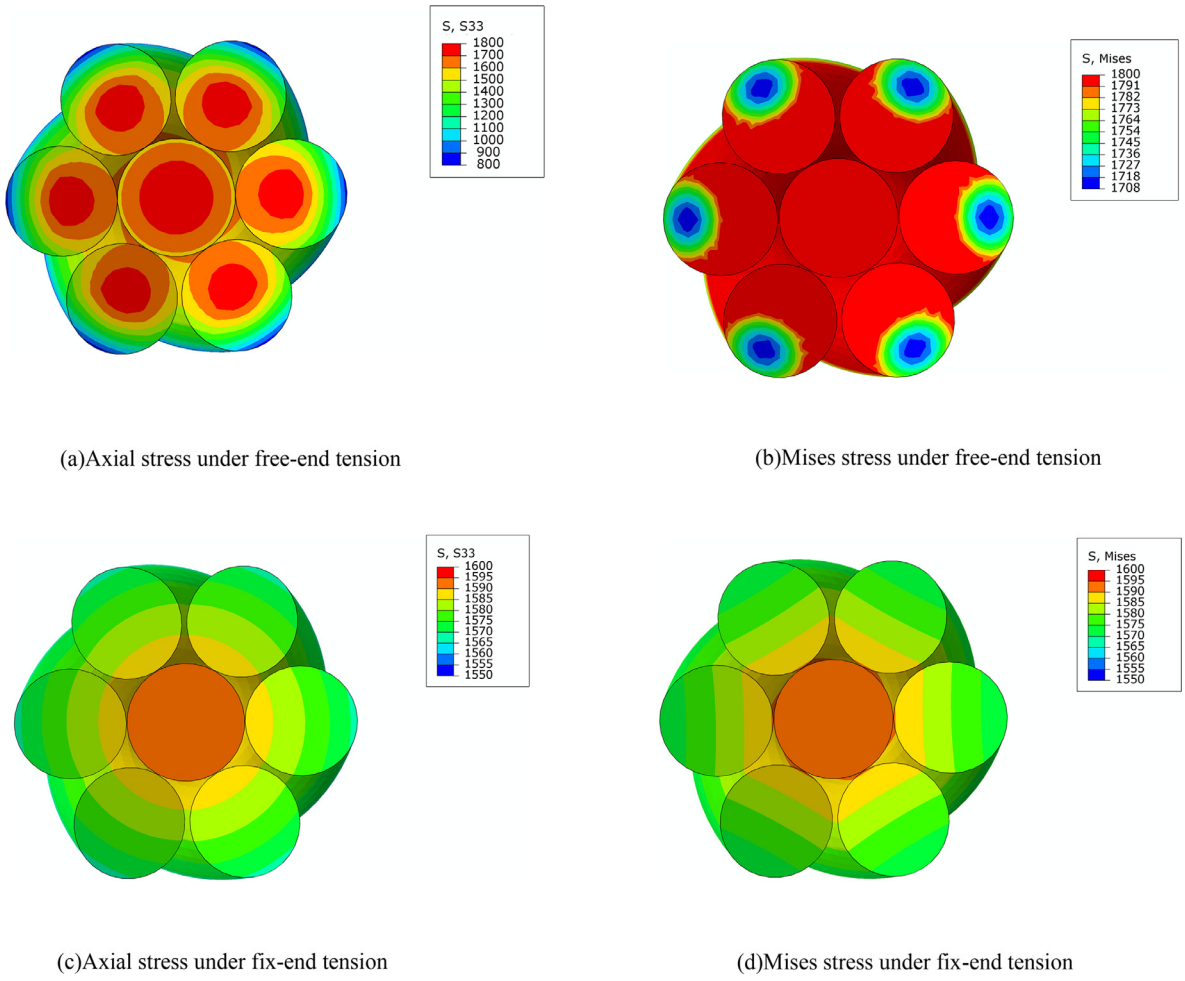

(a)Axial stress under free-end tension

(b)Mises stress under free-end tension

(c)Axial stress under fix-end tension

(d)Mises stress under fix-end tension

Fig. 19. The axial and Von Mises stress distribution of the 1×7 strand under 120 kN.

4.1. Tensile tests of the rope wires

Five specimens of 1.00 mm diameter (constituting the 1×19 strand) and Five specimens of 0.80 mm diameter (constituting the 18×7 wire rope) were prepared for experiment. All the wires have been galvanized with a zinc surface and their lengths were 150 mm. Tensile tests were carried out on an universal servo-hydraulic machine (Instron 8801) with load capacity of 50 kN, measuring elongation with an extensometer having a gauge length equal to 25 mm. Special clamping method was adopted to prevent the wires breaking at the fixed ends. Tests were carried out in displacement control with a crosshead speed of 2 mm/min at room temperature. The average representative σ - ε curves are shown in Fig. 8 and principal tensile parameters are reported in Table 1.

4.2. Surface strain measurement

For experimental tests, not much data are reported in the literature (Nawrocki and Labrosse, 2000). The global response results can be found for simple straight strands in the paper of Utting and Jones (1987a,b) and for multi-strand ropes in the paper of Elata et al. (2004) and Fontanari et al. (2015). However, the data of local strain or stress measurement is still limited. Due to complex structure of wire ropes, strain gauge tests can be only carried out on wires of relatively large diameters, like the work of Knapp and Shimabukuro (2009). Different from conventional extensometry that gives a strain averaged over a single gage length, DIC is a powerful non-contact measuring technique that gives the full-field strain distribution by tracking the specular pattern on the surface of a specimen. As the rope surface is not a flat plane, 3D-DIC carried out with two cameras is needed to get the spatial deformation of the wires.

The experimental setup is shown in Fig. 9. The rope ends were held in a tapered socket by means of a cast resin cone and the sockets were clamped by steel grips, resulting in an axial free length of 300 mm. The specimen was loaded uniaxially at a rate of 20 kN/min by a MTS 810 device with load capacity of 50 kN. A special clamp was designed to keep the rope from rotating, so the cameras can capture corresponding images from one step to the next.

The ARAMIS 3D deformation measurement supported by GOM company (Germany) is adopted to obtain the surface strain of ropes. Optical imaging for 3D-DIC was performed from the front of the specimen as shown in Fig. 7. The two CCD cameras with 2448×2048 grayscale resolution were controlled remotely by a computer to capture images at a rate of 5 frames per sec. The collected images are stored in TIF format for further processing with the ARAMIS 6.2 photogrammetry software (ARAMIS 6.2).

The accuracy of the DIC measurements is especially dependent on the quality of the surface pattern. To facilitate measurements with the photogrammetry system, adequate contrast in the grayscale and surface pattern on the specimen surface is required. In order to create a high-quality pattern on the specimen surface, the ropes were sprayed by a white paint to obtain a white background. Next, black speckles were randomly sprayed by an airbrush

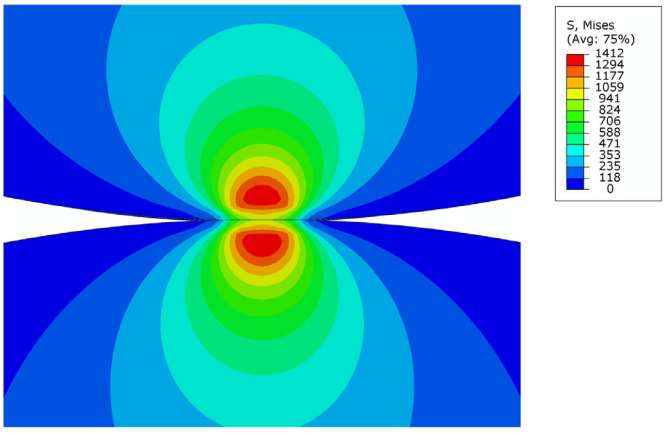

(a) $\varepsilon_t = 0.008, \tau_t = 0\ \text{rad/mm}$

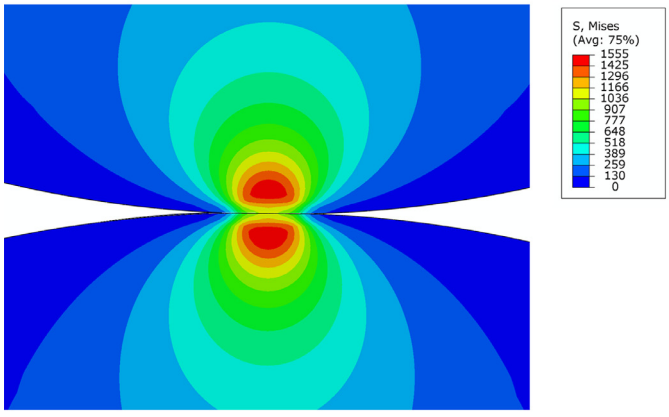

(b) $\varepsilon_t = 0, \tau_t = 0.008\ \text{rad/mm}$

Fig. 20. Contact stress simulation of the 1×7 strand under different loading conditions.

which can change the size of its nozzle and the paint pressure. The resulting speckle pattern on a 1×19 strand is shown in Fig. 9.

5. Results and discussion

5.1. Model implementation and validation

A 7×7 multi-strand rope (usually named as independent wire rope core, i.e. IWRC) is first taken into consideration to elucidate the solution process of the present elastic-plastic model. The geometric properties adopted for the rope are listed in Table 2 and the wire material property obeys the bi-linear constitutive law: Young's modulus $E = 188000\ MPa$, plastic modulus $E_p = 24600\ MPa$, yield stress $\sigma_{p0.2} = 1540\ MPa$, ultimate tensile stress $\sigma_m = 1800\ MPa$ and the Poisson effect is ignored. When the rope is tensioned to $\varepsilon_t = 0.01$ ($\tau_t = 0$), for example, according to the analysis in Section 2.2, its outer strands are subjected to tension ($\xi_{strand} = 0.00899$), torsion ($\tau_{strand} = -0.000232\ \text{mm}^{-1}$) and bending ($\rho_{strand} = 5740\ \text{mm}$) at the same time. Then the outer strand can be geometrically treated as the description in Section 2.1. After the deformation analysis in Section 3.1, the local curvatures and twist of the wires is obtained. Results are shown in Fig. 10 for both lang lay and regular lay structures. The local curvatures and twist varies periodically along the rope axis, so within rope cross sections of each period the strain and stress distribution is different. The tensile strain ξ of an outer wire in an outer strand is 0.00817 and 0.00853 for lang lay and regular lay configurations respectively, according to Eq. (13). The difference of the local deformation parameters between lang lay and regular lay wires is due to their opposite helix direction within the outer strands.

Based on the four local deformation parameters ($\Delta\kappa$, $\Delta\kappa'$, $\Delta\tau$ and ξ), the strain of the grid points on the wire cross section is calculated via Eqs. (14) to (17) Then after the iteration computation, elastic-plastic stresses of the points can be obtained and subsequently the forces and moments over the cross section are integrated through Eqs. (21) and (22). Finally the force and torque of the rope can be gotten by projecting the local forces and moments of wire cross sections to the global coordinate system. Fig. 11 exhibits the axial force of the 7×7 rope varying with the axial elongation, when both ends of the rope are restrained. The FEM results from Erdonmez and Imrak (2011) are also given for comparison. Within the elastic region, the forces predicted by the present model coincide with results of Costello (1990). When the rope axial strain ε_t is up to 0.01, the forces of the lang lay and regular lay ropes have both turned into the plastic range and the results agree well with the simulation of Erdonmez and Imrak (2011).

Another simpler case is the elastic-plastic response of a 1×7 strand, whose geometric character is also given in Table 2 and the wire material property obeys the same bi-linear constitutive law. The related experiments were carried out by of Utting and Jones (1987a,b) and results have been widely used to demonstrate the accuracy of other authors' models, like aforementioned work of Jiang et al., (1999), Ghoreishi et al., (2007) and Foti and Martinelli (2016a). Fig. 12 shows the axial force and torsional moment varying with the axial strain of the 1×7 strand. As we can see, the global response of the ropes predicted by the present model coincides with the experimental and finite element results not only in the elastic region but also up to the plastic extent. The axial force is a little higher than the data of other authors within the plastic region but not much (less than 6%). Therefore, the present model gives correct elastic-plastic prediction of axial-torsional behavior of ropes.

5.2. Local strain of the ropes

The force-displacement curves of the 1×19 strand and the 18×7 rope are shown in Fig. 13. The strand is loaded monotonously until final break happens, while the rope is tensioned to 43 kN, holding for 10 s and then unloaded to zero. The breaking force of 1×19 strand is about 18.3 kN. The elastic modulus of the 18×7 cable in the early load stage, during subsequent loading upon 10 kN and over the unloading process differ with each other (Fig. 13b). That is because the total elongation of the wire cable under load consists of two parts: the constructional stretch and the material stretch. In the early load stage, the constructional stretch is prominent to minimize the clearances between wires through compression of the core and outer strands and it will stay even after the removal of the external load, while material stretch will disappear (Zhu and Meguid, 2007). For the simple 1×19 straight strand, the clearance within the rope is much less than in the multi-strand 18×7 cable, so the force is directly applied on the wire material with less constructional effect. The reader may notice that the force is not zero at the start of the experiment. This little load (about 0.2 kN) is taken to make the ropes straight to facilitate the measurement of surface strain through DIC method.

Fig. 14 gives the axial tension strain ε_{33} of the 1×19 strand from 3D-DIC test. As first, the strain increases linearly with the axial force. When the force is beyond about 9 kN, the increase rate of the strain becomes bigger and bigger, since the strand has turned into the plastic state. The distribution of strain on the outer surface of the strand is uniform due to the helical symmetry of the wires. Our elastic-plastic estimation of wire deformation and stress

Table 3
Comparison of line contact results of the 1×7 simple strand.

	Hertz's theory	Present simulation	Meng et al., (2016)
$\varepsilon_t = 0.008$, $\tau_t = 0$ rad/mm			
Maximum contact pressures (MPa)	2428	2492	2550
Maximum Mises stresses (MPa)	——	1412	1450
$\varepsilon_t = 0$, $\tau_t = 0.008$ rad/mm			
Maximum contact pressures (MPa)	2849	2739	2820
Maximum Mises stresses (MPa)	——	1555	1610

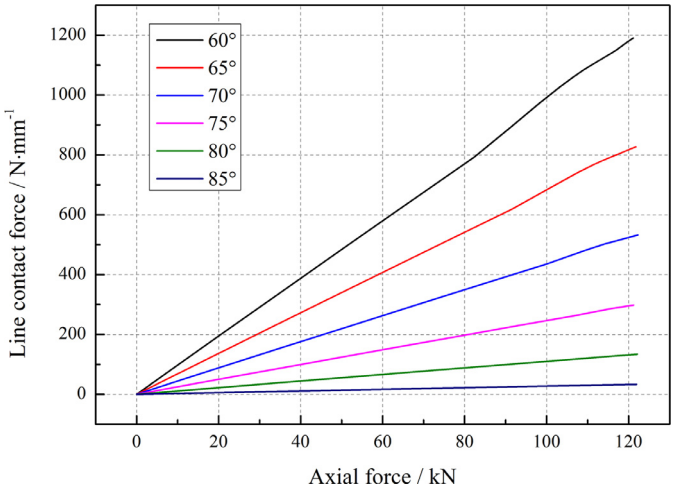

Fig. 21. Contact force estimation of 1×7 strands with different helix angles under fix-end tension.

is shown in Fig. 15. As we can see, each sprial wire is not only subjected to axial tension but also to bending against the rope center. When the strand is loaded to 17 kN, it has turned into the plastic deformation stage. The surface strain ε_{33} of our calculation is 0.64%, while the measurement through 3D-DIC in Fig. 14(a) is 0.61% (average value). The discrepancy between the two methods is less 5%, which proves the accuracy of the present model.

The 3D-DIC result of ε_{33} along the 18×7 multi-strand rope is shown in Fig. 16. The strain always increases linearly with the axial force as the maximum force loaded on the rope (about 43 kN) does not exceed its elastic limit. The distribution of surface strain of the rope is not so uniform as the 1×19 strand. This may result from the lack of helical symmetry along the outer wires of spiral strands. As the analyses to Fig. 10, the deformation of double-helix wires varies with their positions within the rope. Our elastic-plastic estimation of wire deformation and stress of the 18×7 rope loaded to 43 kN is shown in Fig. 17. Also, each helix wire is subjected to bending against the corresponding strand center or rope center. The surface strain ε_{33} of our simulation is 0.51%, which agrees well with the measurement of 0.47% (average value) through 3D-DIC in Fig. 16(a).

5.3. Stresses under different loading conditions

Take the elastic-plastic 1×6 strand introduced in Section 5.1 into consideration. Stresses under three different loading conditions or boundary conditions are analyzed: fix-end tension ($\tau_t = 0$), free-end tension ($\tau_t \neq 0$) and fix-end torsion ($\varepsilon_t = 0$). As wire ropes are mainly used to bear the axial force, the stress distributions at the same axial tension are compared to estimate the wire yielding and failure behavior.

Fig. 18 interprets the Von Mises equivalent stress distribution under different loading conditions with axial force of 75 kN. One can clearly find that the fix-end torsion case (Fig. 18(c)) leads to much bigger stress and the wire failure has happened on the outer surface of the strand (where the Mises equivalent stress has reached ultimate stress σ_m). In contrast, the two tension cases generate their biggest stress on the center wire and the inner side of the outer wires. The wires subjected to free-end case (Fig. 18(b)) have begun to yield while those under fix-end case (Fig. 18(a)) are still in the elastic region. The deformation of outer wires under fix-end case is a combine of axial tension and bending against the rope center while outer wires under free-end case is subjected to additional axial torsion, which is in accordance with the external boundary restraint at the rope ends.

The axial and Von Mises stress distributions obtained through the proposed analytical model under 120 kN are shown in Fig. 19. Only the fix-end tension case and the free-end tension case can be analyzed since the strand under fix-end torsion load has come to its full failure before 120 kN (see the aforementioned illustration). As the strands are subjected to the same axial force, the average axial stress through the cross section should be the same. However, the varying range of the axial stress under free-end tension (Fig. 19(a)) is much bigger than that under fix-end tension (Fig. 19(c)). For the Von Mises equivalent stresses, we can see that a wide extent of yielding even failure has happened on wires under free-end condition due to their torsional shear stresses. As a comparison, the fix-end tension wires mainly undergo limited yielding and no failure has appeared. In this sense, the end rotation always goes against the rope service security. Nevertheless, the wire stress state is also closely related to the localized contact status between neighborhood wires, which will be elucidated in the next section.

5.4. Contact analysis of metallic strands

Firstly, in order to verify the accuracy of our contact computation, the line contact of the 1×7 strand in Table 2 is considered. We ignore the plastic deformation at first for the comparison with the results from the prevalent Hertz contact theory (elaborated in detail by Johnson (1985)) and the elastic model of Meng et al., (2016). The Young's modulus is temporarily taken as 197,900 MPa here since this value was adopted by Meng et al., (2016). Fig. 20(a) and (b) show the Von Mises equivalent stress distribution of the contact wires when the strand is subjected to axial tension $\varepsilon_t = 0.008$, $\tau_t = 0$ rad/mm and axial torsion $\varepsilon_t = 0$, $\tau_t = 0.008$ rad/mm respectively. The maximum value appears at the location a little below the contact plane. As displayed in Table 3, the results from our simulation show good agreement with those from the Hertz theory and the analysis of Meng et al., (2016). Therefore, our model is validated for the wire contact problems.

Then we reconsider the bi-linear elastic-plastic constitutive law introduced in Section 5.1 for the 1×7 strand. Fig. 21 shows line contact force of strands with different helix angles when the strands are subjected to axial tension ($\tau_t = 0$). One can clearly find that as the axial load increases, the contact force between the core wire and the outer wire increases accordantly. The bigger helix angle leads to larger contact force when the axial loads are the same,

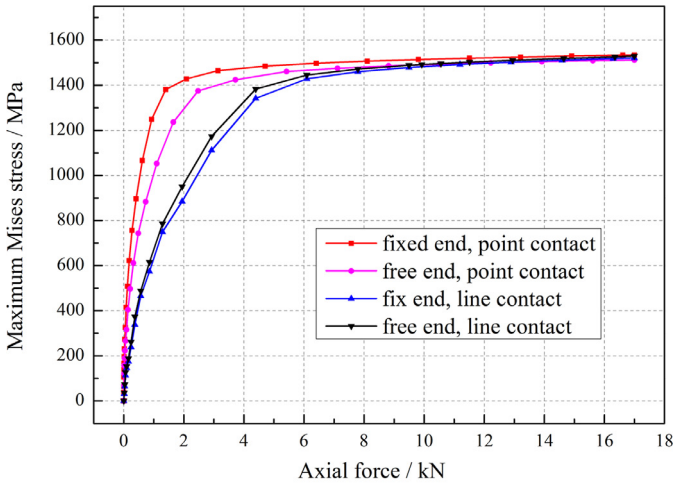

(a) Maximum Mises stress

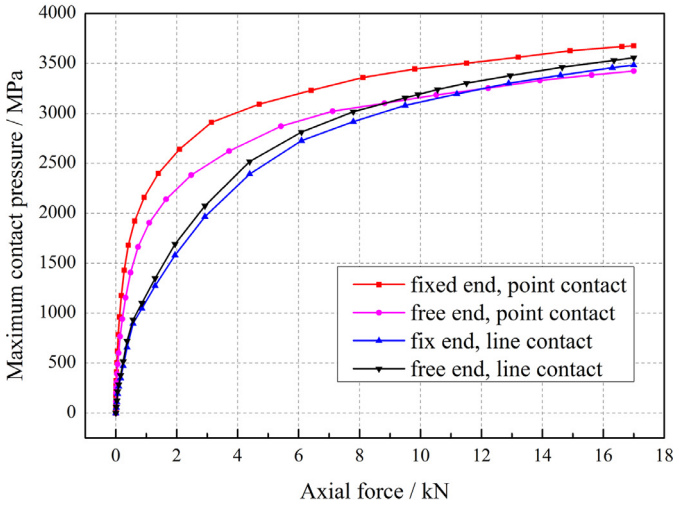

(b) Maximum contact pressure

Fig. 22. Line contact and point contact simulation results of the 1×19 strand under different loading conditions.

no matter in the elastic region or the plastic region. So one may choose a high helix angle strand to avoid the contact failure or reduce the wear damage. However, the helix angle can't be too large as the strand will become too loose to keep its structural stability. Therefore, a moderate value is more preferable.

Finally the 1×19 multi-layer strand is taken into account to analyze the different wire contact type, i.e. line contact and point contact. Also, the results of two different loading conditions (fixed end tension and free end tension) are given for comparison. Fig. 22(a) gives the maximum Mises stress of the contact wires varying with the axial force. As we can see, for both loading cases the point contact leads to much larger stress than the line contact, due to its smaller contact area. The local material of the wire starts to yield even at about 1 kN (for point contact in fix end case), which is far less than the rope global yielding force. Usually, constraining both ends will lead to the constriction of the rope, which reduces the clearance within the wires and generates more contact forces. As a consequence the point contact stress under fixed end condition is bigger than that under free end condition. However, this is not the situation for line contact. Both the line contact stress and line contact pressure (shows in Fig. 22(b)) are inversely a little larger in free end case, though much smaller press from outer layer generates. One should notice that the two layers of the 1×19 strand are with opposite helical direction (Fig. 6). So when the whole strand undergoes negative rotation under free end tension, the inner layer actually suffers positive torsion, which means the inner layer constricts. As the line contact happens between the central wire and the inner layer wire, that is why the line contact is more prominent under free end condition. Another interesting finding is under free end loading, the line contact pressure and stress exceed the point contact ones when the axial force is greater than 9 kN. This indicates that under free end tension the point contact is more dominant in the elastic region of the rope, while the line contact becomes significant when yielding begins to happen on the strand, at least for the present rope structure and material.

6. Conclusions

The paper investigates the elastic–plastic behavior of wire ropes under axial tension and torsion loads. Based on the frictionless hypothesis and treating one individual wire as a curved thin rod, a new mechanical formulation to compute the local tension, bending and torsion deformation of wires is introduced first, especially for double-helix wires in multi-strand ropes. Then the strain of points on a wire cross section is derived and a general algorithm for the incremental plasticity is adopted to get the elastic-plastic stresses. Besides, a new procedure to estimate the contact forces is put forward for both the line contact and point contact conditions within the strands. The global forces and torques of the ropes predicted by the present model coincide with the experimental and finite element results of previous authors. Details of the surface strain fields of the 1×19 strand and 18×7 non-rotating rope are captured by 3D-DIC technique and the results agree well with our elastic-plastic estimation. Our analytical model can give an acceptable estimate of the stress distribution over the wire cross sections and a good prediction of the global response for wire ropes.

Different tension and torsion conditions lead to different yielding and failure behavior of wire strands. We found that, on the one hand, the rotation of ropes (no matter its positive or negative) will increase the overall stress level within the wire cross section due to the additional torsional stresses to the wires. On the other hand, restraining the rope ends leads to higher contact stress (especially for the point contact wires) due to the constriction of the rope. So a full understanding of rope inner state should be a combine of global stress estimation and the localized stress analysis of the contact area. Increasing the helix angle moderately can reduce the contact pressure of strand wires to a certain extent. However, the contact problem of a multi-strand rope is still difficult to deal with since its structure is much more complex than the straight strand, which deserves a further study in the later work.

Acknowledgments

The work is supported by the National Key Research and Development Program of China (No. 2017YFB0702003), the Strategic Priority Research Program of the Chinese Academy of Sciences (Grant Nos. XDB22040302, XDB22040303), The Natural Science Foundation of China (Grants No. 11572324), and the Key Research Program of Frontier Sciences (Grant No. QYZDJSSW-JSC011).

References

Argatov, I., 2011. Response of a wire rope strand to axial and torsional loads: asymptotic modeling of the effect of interwire contact deformations. Int. J. Solids Struct. 48, 1413–1423.
Belytschko, T., Liu, W.K., Moran, B., 2000. Nonlinear Finite Elements For Continua and Structures. John Wiley & Sons Ltd, Chichester, England.
Cardou, A., Jolicoeur, C., 1997. Mechanical models of helical strands. Appl. Mech. Rev. 50, 1–14.
Costello, G.A., 1990. Theory of Wire Rope. Springer–Verlag, New York.

Costello, G.A., Philips, J.W., 1976. Effective modulus of twisted wire cables. J. Eng. Mech. Division 102, 171–181 ASCE.
Cruzado, A., Leen, S.B, Urchegui, M.A., Gómez, X., 2013. Finite element simulation of fretting wear and fatigue in thin steel wires. Int. J. Fatigue 55, 7–21.
Cruzado, A., Urchegui, M.A., Gómez, X., 2014. Finite element modeling of fretting wear scars in the thin steel wires: Application in crossed cylinder arrangements. Wear 318, 98–105.
Elata, D., Ashkenazi, R., Weiss, M., 2004. The mechanical behaviour of a wire rope with an independent wire rope core. Int. J. Solids Struct. 41, 1157–1172.
Erdonmez, C., Imrak, C.E., 2011. A finite element model for independent wire rope core with double helical geometry subjected to axial loads. Sadhana–Acad. Proc. Eng. Sci. 36 (6), 995–1008.
Feyrer, K., 2007. Wire ropes: tension, endurance, reliability. Springer.
Fontanari, V., Benedetti, M., Monelli, B.D., 2015. Elastic–plastic behavior of a Warrington–Seale rope: Experimental analysis and finite element modeling. Eng. Struct. 82 (0), 113–120.
Foti, F., de Luca di Roseto, A., 2016a. Analytical and finite element modelling of the elastic–plastic behaviour of metallic strands under axial–torsional loads. Int. J. Mech. Sci. 115–116, 202–214.
Foti, F., Martinelli, L., 2016b. An analytical approach to model the hysteretic bending behavior of spiral strands. Appl. Math. Model. 40, 6451–6467.
Foti, F., Martinelli, L., 2016c. Mechanical modeling of metallic strands subjected to tension, torsion and bending. Int. J. Solids Struct. 91, 1–17.
Frigerio, M., Buehlmann, P.B., Buchheim, J., Holdsworth, S.R., Dinser, S., Franck, Ch.M., Papailiou, K., Mazza, E., 2016. Analysis of the tensile response of a stranded conductor using a 3D finite element model. Int. J. Mech. Sci. 106, 176–183.
Ghoreishi, S.R., Messager, T., Cartraud, P., Davies, P., 2007. Validity and limitations of linear analytical models for steel wire strand under axial loading, using a 3D FE model. Int. J. Mech. Sci. 49 (11), 1251–1261.
Gnanavel, B.K., Gopinath, D., Parthasarathy, N.S., 2010. Effect of friction on coupled contact in a twisted wire cable. J. Appl. Mech. 77 (11), 024501.
Gnanavel, B.K., Parthasarathy, N.S., 2011. Effect of interfacial contact forces in radial contact wire strand. Arch. Appl. Mech. 81, 303–317.
Gnanavel, B.K., Parthasarathy, N.S., 2012. Effect of interfacial contact forces in single layer cable assemblies. Int. J. Mech. Mater. Design 8, 183–195.
Hruska, F.H., 1952a. Radial forces in wire ropes. Wire Wire Prod. 27, 459–463.
Hruska, F.H., 1952b. Tangential forces in wire ropes. Wire Wire Prod. 28, 459–463.
Jiang, W.G., Yao, M.S., Walton, J.M., 1999. A concise finite element model for simple straight wire rope strand. Int. J. Mech. Sci. 41 (2), 143–161.
Jiang, W.G., Warby, M.K., Henshal, J.L., 2008. Statically indeterminate contacts in axially loaded wire strand. Eur. J. Mech.–A/Solids 27 (1), 69–78.
Johnson, K.L., 1985. Contact Mechanics. Cambridge University Press, Cambridge.
Judge, R., Yang, Z., Jones, S.W., Beattie, G., 2012. Full 3D finite element modelling of spiral strand cables. Constr. Building Mater. 35, 452–459.
Knapp, R., Shimabukuro, T., 2009. Cable testing in tension, twist and bending. The Nineteenth International Offshore and Polar Engineering Conference, International Society of Offshore and Polar Engineers.
Kumar, K., Botsis, J., 2001. Contact stresses in multilayered strands under tension and torsion. J. Appl. Mech. 68, 432–440.
Kumar, K., Cochran, J.J.E., Cutchins, J.A., 1997. Contact stresses in cables due to tension and torsion. J. Appl. Mech. 64, 935–939.
Lanteigne, J., 1985. Theoretical estimation of the response of helically armored cables to tension, torsion, and bending. J. Appl. Mech. 52, 423–432.
LeClair, R.A., 1991. Axial response of multilayered strands with compliant layers. J. Eng. Mech. 117, 2884–2903 ASCE.
Lee, W.K., 1991. An insight into wire rope geometry. Int. J. Solids Struct. 28 (4), 471–490.
Lévesque, F., Goudreau, S., Cloutier, L, 2011. Elastic–plastic microcontact model for elliptical contact areas and its application to a treillis point in overhead electrical conductors. J. Tribol.-Trans. ASME 133 (1), 011401.
Love, A.E.H., 1944. A Treatise on the Mathematical Theory of Elasticity, Chaps. 18 and 19. Dover Publications, New York.
Meng, F., Chen, Y., Du, M., Gong, X., 2016. Study on effect of inter-wire contact on mechanical performance of wire rope strand based on semi-analytical method. Int. J. Mech. Sci. 115–116, 416–427.
Nawrocki, A., Labrosse, M., 2000. A finite element model for simple straight wire rope strands. Comput. Struct. 77, 345–359.
Páczelt, I., Beleznai, R., 2011. Nonlinear contact–theory for analysis of wire rope strand using high–order approximation in the finite element. Comput. Struct. 89, 1004–1025.
Spak, K., Agnes, G., Inman, D., 2013. Cable modeling and internal damping developments. Appl. Mech. Rev. 65, 010801–010818.
Stanova, E., Fedorko, G., Fabian, M., Kmet, S., 2011a. Computer modelling of wire strands and ropes. Part I: theory and computer implementation. Adv. Eng. Softw. 42, 305–315.
Stanova, E., Fedorko, G., Fabian, M., Kmet, S., 2011b. Computer modelling of wire strands and ropes. Part II: finite element–based applications. Adv. Eng. Softw. 42, 322–331.
Usabiaga, H., Pagalday, J.M., 2008. Analytical procedure for modeling recursively and wire by wire stranded ropes subjected to traction and torsion loads. Int. J. Solids Struct. 45, 5503–5520.
Utting, W.S., Jones, N., 1987a. The response of wire rope strands to axial tensile loads. Part I: Experimental results and theoretical predictions. Int. J. Mech. Sci. 29 (9), 605–619.
Utting, W.S., Jones, N., 1987b. The response of wire rope strands to axial tensile loads. Part II: Comparison of experimental results and theoretical predictions. Int. J. Mech. Sci. 29 (9), 621–636.
Velinsky, S.A., Andewn, G., Costello, G., 1984. Wire rope with complex cross sections. J. Eng. Mech. Div. 110 (3), 380–391 ASCE.
Wang, D., Zhang, D, Ge, S., 2013. Finite element analysis of fretting fatigue behavior of steel wires and crack initiation characteristics. Eng. Failure Anal. 28, 47–62.
Xiang, L., Wang, H.Y., Chen, Y., Guan, Y.J., Wang, Y.L., Dai, L.H., 2015. Modeling of multi–strand wire ropes subjected to axial tension and torsion loads. Int. J. Solids Struct. 58 (0), 233–246.
Zhu, Z.H., Meguid, S.A., 2007. Nonlinear FE-based investigation of flexural damping of slacking wire cables. Int. J. Solids Struct. 44 (16), 5122–5132.